



Combinatorial atomistic-to-AI prediction and experimental validation of heating effects in 350 F supercapacitor modules

Bo, Z., Li, H., Yang, H., Li, C., Wu, S., Xu, C., Xiong, G., Mariotti, D., Yan, J., Cen, K., & Ostrikov, KK. (2021). Combinatorial atomistic-to-AI prediction and experimental validation of heating effects in 350 F supercapacitor modules. *International Journal of Heat and Mass Transfer*, 171, 121075. Article 121075. <https://doi.org/10.1016/j.ijheatmasstransfer.2021.121075>

[Link to publication record in Ulster University Research Portal](#)

Published in:

International Journal of Heat and Mass Transfer

Publication Status:

Published (in print/issue): 30/06/2021

DOI:

[10.1016/j.ijheatmasstransfer.2021.121075](https://doi.org/10.1016/j.ijheatmasstransfer.2021.121075)

Document Version

Author Accepted version

General rights

Copyright for the publications made accessible via Ulster University's Research Portal is retained by the author(s) and / or other copyright owners and it is a condition of accessing these publications that users recognise and abide by the legal requirements associated with these rights.

Take down policy

The Research Portal is Ulster University's institutional repository that provides access to Ulster's research outputs. Every effort has been made to ensure that content in the Research Portal does not infringe any person's rights, or applicable UK laws. If you discover content in the Research Portal that you believe breaches copyright or violates any law, please contact pure-support@ulster.ac.uk.

Combinatorial Atomistic-to-AI Prediction and Experimental Validation of Heating Effects in 350 F Supercapacitor Module

Zheng Bo^{a,b}, Haowen Li^{a,b}, Huachao Yang^{a,b,*}, Changwen Li^{a,b}, Shenghao Wu^{a,b}, Chenxuan Xu^{a,b}, Guoping Xiong^c, Jianhua Yan^{a,b}, Kefa Cen^{a,b} and Kostya (Ken) Ostrikov^{d,e,a}

^aState Key Laboratory of Clean Energy Utilization

College of Energy Engineering, Zhejiang University

Hangzhou, Zhejiang Province 310027, China

^bZJU-Hangzhou Global Scientific and Technological Innovation Center

Hangzhou, Zhejiang Province 311215, China

^cDepartment of Mechanical Engineering, The University of Texas at Dallas,

Richardson, TX 75080, USA

^dSchool of Chemistry and Physics and QUT Centre for Materials Science,

Queensland University of Technology (QUT), Brisbane, Queensland 4000, Australia

^eJoint CSIRO-QUT Sustainable Processes and Devices Laboratory,

P. O. Box 218, Lindfield, NSW 2070, Australia

*Email: huachao@zju.edu.cn

Abstract

Accurately predicting thermal behavior is critically important in the real-world thermal management of supercapacitor modules with ultrahigh power and discharging current. In this work, an artificial intelligence (AI) approach based on the improved multiscale coupled electro-thermal model is employed for the first time to accurately predict the thermal behavior of a 350 F supercapacitor module under air-cooling conditions. Different from previous work which used commercial cells, the 350 F supercapacitors are fabricated from our proprietary pilot-scale production line. This approach provides a platform to precisely measure the structural parameters, electrical and thermal properties of electrodes and electrolytes (e.g., the

temperature/current dependent equivalent series resistance and axial/radial thermal characteristics), which can improve the model for characterizing the irreversible heat generation and thermal transport processes. In particular, coupled with molecular dynamics simulations, the molecular origin of entropy is revealed via probing the atomic-level information (e.g., 1D/2D electric double-layer structure, electrical field/potential distributions, areal capacitance and diffusion kinetics) to accurately predict the reversible heat generation. As a consequence, the deviation between our improved model and experimental results is substantially reduced to below 3%. Deep neural network based on the long short-term memory (LSTM) approach is trained to build a temperature database for practical supercapacitor modules under different operating conditions (including charging/discharging currents, cooling airflow rates and cycle duration). This work demonstrates the potential of LSTM deep neural networks in predicting the thermal behavior, which can be broadly used for industry-relevant thermal management applications.

Keywords: Multiscale coupled electro-thermal model; Long Short Term Memory approach; Irreversible and reversible heat; Entropy; Thermal management; 350 F supercapacitor modules.

1. Introduction

Supercapacitors that store electric energy via rapid ion adsorption and separation at the solid/liquid interface [1, 2] have shown major advantages over rechargeable batteries in terms of high power density (> 10 kW/kg), ultrafast charge/discharge rates and wide operational temperature window ($-40\sim 60$ °C) [3, 4]. These beneficial features make supercapacitors a prime candidate for high-power demanding applications, such as uninterruptable power supply, braking energy regeneration (e.g., gantry cranes in maritime port terminals), emergency power support (e.g., emergency exits of commercial airplanes) and aerospace systems. In these typical commercial applications, ultrahigh discharging current (e.g., 200-2000 A) and power (e.g., 50-200 kW) are usually needed, which inevitably result in substantial heat generation and even overheating, seriously threatening the service life time and reliability of supercapacitors. For example, the life cycle of a typical commercial supercapacitor is halved for every 10 °C increment in the working temperature [5]. Thus, precise prediction of the thermal behavior (e.g., temperature rise and distributions) of supercapacitors is becoming particularly important, which is indispensable for thermal management and temperature control.

The heat generation of supercapacitors mainly arises from both irreversible heat and reversible heat [6, 7]. The irreversible heat is generated from Joule effects, while the reversible heat is closely related to the changes of electrolyte entropy, leading to a temperature rise and temperature oscillations, respectively [8-15]. A variety of electro-thermal models combining electrical and thermal models have been developed to predict the heat generation during the charging/discharging process. For example, Li et al. [16] established the electrochemical-thermal coupling model of rectangular stacked-type supercapacitors; the model put forward by Gualous et al. described the temperature distribution inside and outside supercapacitors as a function of the position and time [17]; the electrical and thermal models proposed by Berrueta et al. are based on the equivalent circuits to characterize the voltage and operating temperature of supercapacitors [18].

Unfortunately, significant deviations between experimental observations and theoretical predictions are always observed, because most of the electro-thermal models are based on continuum theory, and the atomic-level information is usually neglected. For example, the

widely used heat generation model by Julia Schiffer et al. [8] ignores the variation of equivalent series resistance (ESR) during the charging/discharging processes, and the volumes of the Helmholtz layer and bulk electrolyte do not take into account molecular-level information. These assumptions make it impossible to accurately describe the entropy change and the shape of temperature wave profile. In order to overcome these limitations, other models mostly focused on the microscopic electric double layer (EDL) structure within the interfacial few nanometer thickness areas. As a prime example, Pilon et al. [19-21] derived first principles models by considering ion diffusion, steric effects and entropy changes of mixing associated with the activity and temperature gradients. However, it is difficult to deduce the practical process parameters from this model. Some attempts to model thermal behaviour were also made via classical density functional theory (DFT) [22]; however, the use of free energy functional is not justifiable when the spatial variations in the diffusion coefficient and temperature become non-negligible.

In addition to individual supercapacitor cells, accurately predicting the thermal behavior of the overall modules is also critically important in the real-world thermal management. A common approach is to experimentally monitor the temperature rise within the modules via thermocouples [14, 17] or calorimeters [6, 23, 24], while it is rather time-consuming and complicated to accurately obtain three-dimensional (3D) temperature distribution and heat generation. With recent advances in artificial intelligence (AI), many AI techniques such as deep neural networks have been used to resolve complex engineering problems [25, 26]. A number of different architectures of neural networks have been evaluated for predicting thermal behavior in supercapacitors, such as standard deep neural networks (DNN) [27, 28], deep recurrent neural networks (RNN) [29], conditional generative adversarial neural networks (cGAN) [30], and deep feedforward neural networks (DFNN) [31]. In comparison with the conventional methods, these AI approaches provide a computationally efficient way for building non-linear, high dimensional mapping with connections between neurons to predict the thermal load and heat transfer characteristics [32-34]. These unique features have led to successful applications of intelligent methods in the design and thermal performance prediction of Li-ion batteries [35-37]. However, this promising route has not yet been applied in the

thermal management of high-power supercapacitors.

In this work, a long short-term memory (LSTM) approach based on the improved multiscale electro-thermal models is for the first time employed to accurately predict the thermal behaviors of a 350 F supercapacitor module under air-cooling conditions. Different from previous work which used commercial cells, 350 F supercapacitors are fabricated using our proprietary pilot-scale production line. As such, the structural parameters, electrical and thermal properties of electrodes and electrolytes can be precisely measured to improve the model for irreversible heat generation and transport. In particular, molecular dynamics simulation (MD) is employed to reveal the atomic-level information of entropy for more accurate prediction of the reversible heat generation. As a result, the deviation between the results of our model and from our experiments is substantially decreased. Finally, deep neural network based on the LSTM approach is trained for predicting the temperatures of supercapacitor modules under different operating conditions.

2. Model Formulation

350 F supercapacitors are fabricated from our supercapacitor assembly production line. The appearance and core region of the 350 F supercapacitor are shown in Fig. 1(a). The modeling approach is based on a one dimensional (1D) electrochemical model and a three dimensional (3D) thermal model.

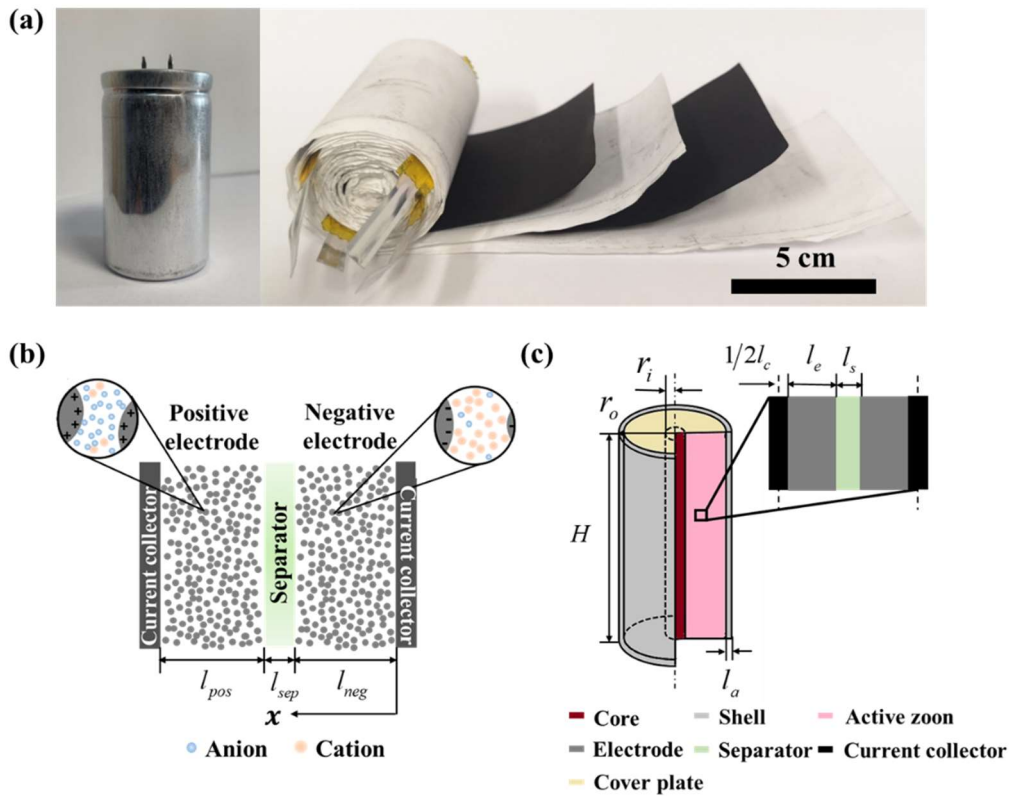


Figure 1. Illustration of (a) 350 F supercapacitor cell and core structure; (b) 1D electrochemical model and (c) 3D thermal model.

2.1 1D Electrochemical Model

Computational domain

A typical supercapacitor cell is composed of a negative electrode, a positive electrode, electrolyte, a separator, and two current collectors as shown in Fig. 1(b). Considering the significantly higher electrical conductivity of current collectors, the electrical potential difference in current collectors is negligible which is eliminated in the computational domain

of electrochemical model. In this work, it is assumed that: 1) porous electrode theory is applied; 2) the unit is completely symmetrical; 3) the Faraday reaction does not exist; 4) the weak electrolyte flow is ignored because of the complete infiltration in porous electrodes and separator; 5) self-discharge and charge redistribution effects are neglected.

Governing equations and Boundary conditions

1) Charge conservation

From the concept of current continuity, a charge conservation equation can be obtained as [61]:

$$\frac{\partial i_s(x,t)}{\partial x} + \frac{\partial i_l(x,t)}{\partial x} = 0 \quad (1)$$

$$\frac{\partial i_l(x,t)}{\partial x} = \delta C_{dl} \frac{\partial (\phi_s(x,t) - \phi_l(x,t))}{\partial t} \quad (2)$$

, where i_s and i_l are the solid phase current density and liquid phase current density (A/m^2), respectively; ϕ_s and ϕ_l are the solid electrical potential and liquid electrical potential, respectively; C_{dl} is the capacitance per interfacial area, and δ is the surface area per unit volume of electrode.

2) Solid charge conservation

The solid current density in electrodes follows Ohm's Law:

$$i_s(x,t) = -\sigma_{elec} \frac{\partial \phi_s(x,t)}{\partial x} \quad (3)$$

In consideration of the porous electrodes, the electronic conductivity can be modified as:

$$\sigma_{elec} = \sigma_s (1 - \varepsilon_{elec})^\beta \quad (4)$$

, where σ_s is the solid phase conductivity, ε_{elec} is the porosity of electrodes, and β is the Bruggeman porosity exponent.

Boundary conditions are set as following:

$$\begin{aligned} \left. \frac{\partial \phi_s(x,t)}{\partial x} \right|_{x=0} &= \frac{i_{app}}{\sigma_{elec}} \\ \left. \frac{\partial \phi_s(x,t)}{\partial x} \right|_{x=l_{neg}+l_{sep}+l_{pos}} &= \frac{i_{app}}{\sigma_{elec}} \end{aligned} \quad (5)$$

$$\left. \frac{\partial \phi_s(x,t)}{\partial x} \right|_{x=l_{neg}, x=l_{neg}+l_{sep}} = 0$$

$$\phi_s(x,t)|_{x=0} = 0$$

, where i_{app} is the applied current density.

3) Liquid charge conservation

The flux of ions N_i is governed by the dilute solution theory, which is closely correlated to the ion migration, diffusion and fluid flow in the electrolyte solution, and the fluid flow is negligible. Based on the Nernst-Planck equation, N_i can be expressed by the following equation:

$$N_i(x,t) = N_{i,trans}(x,t) + N_{i,diff}(x,t) = -\frac{e_i F}{RT} D_i c_i \frac{\partial \phi_l(x,t)}{\partial x} - D_i \frac{\partial c_i(x,t)}{\partial x} \quad (6)$$

, where F is the Faraday's constant, e_i is the charge, R is the universal gas constant, c_i is the ion concentration, D_i is the diffusion coefficient (Einstein-Smoluchowski equation, $D_i = \frac{RTu_i}{|e_i|F}$), u_i

is the migration rate, for a binary electrolyte and $i = 1, 2$.

The relation between liquid current density and ion flux can be described by:

$$i_l(x,t) = F \sum_{i=1}^n e_i N_i(x,t)$$

$$= -\frac{F^2}{RT} \frac{\partial \phi_l(x,t)}{\partial x} \sum_{i=1}^n e_i^2 D_i c_i(x,t) - F \sum_{i=1}^n e_i D_i \frac{\partial c_i(x,t)}{\partial x} \quad (7)$$

Considering the porosity of electrodes and separator, the electrolyte diffusion coefficient within electrodes and separator can be corrected by the following equations:

$$D_{i,elec} = D_i \cdot \varepsilon_{elec}^\beta, D_{i,sep} = D_i \cdot \varepsilon_{sep}^\beta \quad (8)$$

, where ε_{sep} is the porosity of separator.

Boundary conditions are given by:

$$\phi_l(x,t)|_{t=0} = 0$$

$$\left. \frac{\partial \phi_l(x,t)}{\partial x} \right|_{x=0, x=l_{neg}+l_{sep}+l_{pos}} = 0 \quad (9)$$

4) Mass conservation

The mass balance in the electrolyte phase is described as follows:

$$\frac{\partial c_i(x, t)}{\partial t} = -\frac{\partial N_i(x, t)}{\partial x} + R_i \quad (10)$$

, where R_i is the source term (here $R_i = 0$ without chemical reactions).

Boundary conditions are given as below:

$$\begin{aligned} c_1(x, t)|_{t=0} &= c_2(x, t)|_{t=0} = c_0 \\ N_1(x, t)|_{x=0, x=l_{neg}+l_{sep}+l_{pos}} &= N_2(x, t)|_{x=0, x=l_{neg}+l_{sep}+l_{pos}} = 0 \end{aligned} \quad (11)$$

Structural Parameters and Properties

The structural parameters of electrodes and electrolytes measured for the 1D electrochemical modeling are shown in Table 1.

Table 1 Parameters used in the electrochemical model.

| Parameter | Notation | Value |
|---|----------------------|-------------------------|
| Volume fraction for porous electrode | ε_{elec} | 44% |
| Volume fraction for separator | ε_{sep} | 70% |
| Particle radius of positive electrode | r_{pos} | 5 μm |
| Particle radius of negative electrode | r_{neg} | 5 μm |
| Solid phase conductivity | σ_s | 135 S/cm ² |
| Initial electrolyte concentration | c_0 | 1000 mol/m ³ |
| Thickness of separator | l_{sep} | 30 μm |
| Thickness of negative electrode | l_{neg} | 100 μm |
| Thickness of positive electrode | l_{pos} | 100 μm |
| Thickness of collector | l_c | 10 μm |
| Thickness of aluminum shell | l_a | 88 μm |
| Bruggeman porosity exponent | β | 1.5 |
| Specific areal capacitance | C_{dl} | 25.66 F/m ² |
| Surface area per unit volume of electrode | δ | 1800 m ² /g |
| Minimum stop voltage | V_{min} | 0 V |

2.2 3D Thermal Model

Computational domain

The 3D thermal model is shown in Fig. 1(c). The following assumptions are made to simplify the mathematical analysis: 1) thermal conduction is assumed to be the dominated mechanism of heat transfer in the supercapacitor; 2) the heat generation is uniform during the charging and discharging processes; 3) thermal interface resistances at electrode/current collector interface and electrode/electrolyte interface are neglected; 4) the heat transfer of cover plate is considered as adiabatic because its thermal conductivity is rather low compared with other components.

Governing equations and Boundary conditions

Since the structure is symmetrical in 3D cylindrical coordinates, the transient 3D equation can be written as below:

$$\frac{\partial(\rho C_p T(r, z, t))}{\partial t} = \lambda_r \frac{\partial^2 T(r, z, t)}{\partial r^2} + \frac{\lambda_r}{r} \frac{\partial T(r, z, t)}{\partial r} + \lambda_z \frac{\partial^2 T(r, z, t)}{\partial z^2} + q \quad (12)$$

, where $\rho = \frac{\sum \rho_i V_i}{\sum V_i}$, $C_p = \frac{\sum \rho_i C_{pi} V_i}{\rho \sum V_i}$, i is the number of layers, and q refers to the heat

generation per unit volume, $q = \frac{Q_{\text{generation}}}{H \times \pi \times [(r_o - l_a)^2 - r_{\text{core}}^2]}$.

The heat source consists of irreversible and reversible heat generation: $Q_{\text{generation}} = Q_{\text{irrev}} + Q_{\text{rev}}$. The irreversible heat is Joule heat while the reversible heat is due to the entropy change.

The irreversible heat generation is given by the following equation:

$$Q_{\text{irrev}} = I^2 \times ESR \quad (13)$$

, where ESR is the equivalent serial resistance and I is the current load.

The reversible heat generation is expressed as follows:

$$\frac{dQ_{\text{rev}}}{dt} = -T \frac{dS}{dt} \quad (14)$$

Boundary conditions are:

$$\begin{aligned}
T(r, z, t)|_{t=0} &= T_{amb} \\
\lambda_r \frac{\partial T(r, z, t)}{\partial r} \Big|_{r=0} &= 0 \\
-\lambda_a \frac{\partial T(r, z, t)}{\partial r} \Big|_{r=r_o} &= 0 \\
-\lambda_a \frac{\partial T(r, z, t)}{\partial z} \Big|_{z=0} &= 0
\end{aligned} \tag{15}$$

$$-\lambda_a \frac{\partial T(r, z, t)}{\partial r} \Big|_{r=r_o} = h_{total} (T(r, z, t) - T_{amb})$$

$$-\lambda_a \frac{\partial T(r, z, t)}{\partial z} \Big|_{z=0} = h_{total} (T(r, z, t) - T_{amb})$$

, where $h_{total} = h_{conv} + h_{rad}$.

For natural convection,

$$Nu = \frac{h_{conv} \cdot d_o}{\lambda_{air}} = C \cdot Ra^n = C \cdot (\text{Pr} \times Gr)^n \tag{16}$$

, when $10^4 \leq Ra \leq 10^9$, $C = 0.53$ and $n = 1/4$; when $10^9 \leq Ra \leq 10^{13}$, $C = 0.13$ and $n = 1/3$; d_o is the outside diameter, and λ_{air} is the thermal conductivity of air.

For the radiation part,

$$\begin{aligned}
\varepsilon \sigma (T_s^4 - T_{amb}^4) &= h_{rad} (T_s - T_{amb}) \\
h_{rad} &= \varepsilon \sigma (T_s - T_{amb}) (T_s^2 + T_{amb}^2)
\end{aligned} \tag{17}$$

, where ε is the surface emissivity and σ is the Stefan-Boltzmann constant.

Parameters and Properties

The related parameters and properties of materials are listed in Table 2.

Table 2 Material properties.

| Material | Property | Symbol | Value |
|------------------|------------------------|----------|-----------------------|
| Activated carbon | Density | ρ_e | 843 kg/m ³ |
| | Specific heat capacity | C_{pe} | Fig. 3(a) |

| | | | |
|-----------|------------------------|-----------------------|------------------------|
| | Thermal conductivity | λ_e | Fig. 3(a) |
| | Density | ρ_s | 415 kg/m ³ |
| Cellulose | Specific heat capacity | C_{ps} | Fig. 3(b) |
| | Thermal conductivity | λ_s | |
| | Density | ρ_a/ρ_c | 2700 kg/m ³ |
| Aluminum | Specific heat capacity | C_{pa}/C_{pc} | 898.15 J/(kg·K) |
| | Thermal conductivity | λ_a/λ_c | 237 W/(m·K) |

2.3 Artificial Neural Networks

Artificial neural networks (ANN) are a type of deep learning algorithms that model the non-linear relationship between the input and output vectors through multi-layered neurons. Fig. 2(a) presents the ANN model structure consisting of one input layer, some hidden layers and one output layer. The deep learning algorithm implemented in this study is LSTM, which is a special form of gated recurrent neural network (RNN) for dealing with sequential data. Compared with the basic RNN, LSTM aims to solve the problem of vanishing or exploding gradients by introducing three additional gates and a memory cell [38]. A schematic of the LSTM unit is presented in Fig. 2(b). It contains a forget gate, an external input gate, an output gate and a memory cell. Two gates are designed to control the amount of information in the memory cell state (Eq. (18)). One is the forget gate (Eq. (19)) that determines the amount of information at the previous moment needs to be passed to the next time step; the other is the external input gate (Eq. (20)), which determines the amount of input at the current moment saved to the cell state. The LSTM unit also designs an output gate (Eq. (21)) to control the exported information. The final output on the time series is determined by the combined cell state and output gate (Eq. (22)) [39, 40].

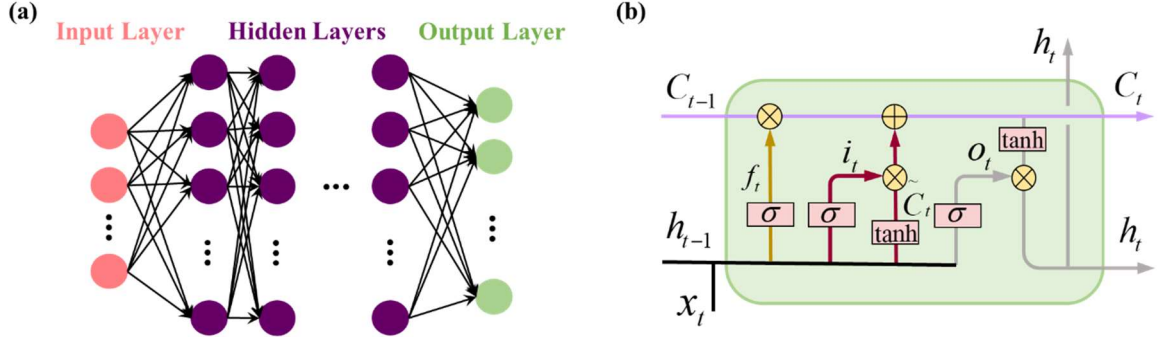


Figure 2. Schematic diagram of (a) multi-layered deep neural network and (b) LSTM cell.

$$C_t = f_t \cdot C_{t-1} + i_t \cdot \tilde{C}_t \quad (18)$$

$$f_t = \sigma(W_f \cdot [h_{t-1}, x_t] + b_f) \quad (19)$$

$$i_t = \sigma(W_i \cdot [h_{t-1}, x_t] + b_i), \tilde{C}_t = \tanh(W_C \cdot [h_{t-1}, x_t] + b_C) \quad (20)$$

$$o_t = \sigma(W_o \cdot [h_{t-1}, x_t] + b_o) \quad (21)$$

$$h_t = o_t \cdot \tanh(C_t) \quad (22)$$

, where $\sigma(x) = \frac{1}{1 + \exp(-x)}$ and $\tanh(x) = \frac{e^{2x} - 1}{e^{2x} + 1}$; C_t is the memory cell value, $x^{(t)}$ is the

input, \tilde{C}_t is the candidate value and $h(t)$ is the activation value of hidden layers at time step t . W_f, W_i, W_o, W_C are the weight matrices to calculate the forget gate, input gate, output gate, and memory candidate, respectively; b_f, b_i, b_o, b_C are the bias vectors to calculate the forget gate, input gate, output gate, and memory candidate, respectively. $[h_{t-1}, c]$ denotes concatenate h_{t-1} and x_t vertically, f_t, i_t, o_t are the forget gate, input gate and output gate, respectively.

The algorithm to solve the network is the Adam optimization algorithm. The initial learning rate is 0.01. The approach is developed using the Keras API in Python 3 on a Tensorflow backend. To prevent the over-fitting, the LSTM approach is regularized using weight decay regularization and early-stopping.

2.4 MD Simulation

MD simulations are performed using the Large-scale Atomic/Molecular Massively

Parallel Simulator (LAMMPS) program. The temperature of electrolyte is maintained at 300 K, controlled by the Nose-Hoover thermostat with a damping parameter of 0.10 ps. The Coulombic and van der Waals forces in the real space are calculated with a cutoff of 12.0 Å. The long-range Coulombic interactions are handled by the particle-particle particle-mesh (PPPM) algorithm with an accuracy of 10^{-5} . All MD simulations are equilibrated for 10 ns with a time step of 1 fs, followed by 5 ns to save the trajectories every 1 ps.

3. Results and Discussions

3.1 Improved Electro-Thermal Model

3.1.1 Correlation of ESR and thermal characteristics

In the conventional irreversible heat model, the ESR of supercapacitors is considered as a constant value during the charging/discharging processes, while it is practically dependent on the operating temperature and conditions (e.g., discharging current) [14, 41]. In this work, we have been able to measure in real-time the change of the *ESR* during the 350 F supercapacitor operation period. On the basis of experimental results, we have been able to correlate *ESR* to the operating temperature T (K) and current I (A) and we have consequently produced an analytical expression derived from a fitting procedure:

$$ESR = 0.05035 - 0.002151 \times I - 0.000126 \times T + 0.000006304 \times T \times I \quad (23)$$

Based on this, the irreversible heat generation can be calculated as:

$$\begin{aligned} Q_{irrev} &= I^2 \times (0.05035 - 0.002151 \times I - 0.000126 \times T + 0.000006304 \times T \times I), \\ &= 0.05035I^2 - 0.002151I^3 - 0.000126I^2T + 0.000006304I^3T \end{aligned} \quad (24)$$

which is to be used in our 3D model in replacement of equation 13.

In addition, thermal properties also play a key role in determining the thermal model. In this paper, the thermal characteristics (including thermal conductivity and specific heat capacity) of electrodes (Fig. 3(a)) and separator (Fig. 3(b)) are measured by a flash method via Netzsch LFA457 instrument. The axial thermal conductivity for the entire calculation domain is calculated as:

$$\lambda_z = \frac{\lambda'_z \left[(r_o - l_a)^2 - r_{core}^2 \right] + \lambda_a \left[r_o^2 - (r_o - l_a)^2 \right]}{r_o^2 - r_{core}^2} \quad (25)$$

, and the radial thermal conductivity of whole computational domain can be determined as:

$$\lambda_r = \frac{\ln\left(\frac{r_o}{r_{core}}\right)}{\frac{1}{\lambda'_r} \ln\left(\frac{r_o - l_a}{r_{core}}\right) + \frac{1}{\lambda_a} \ln\left(\frac{r_o}{r_o - l_a}\right)} \quad (26)$$

, where λ'_z and λ'_r are the axial thermal conductivity and radial thermal conductivity for the active zoon, respectively. The detailed calculation of λ'_z and λ'_r is available in the Supporting

Information.

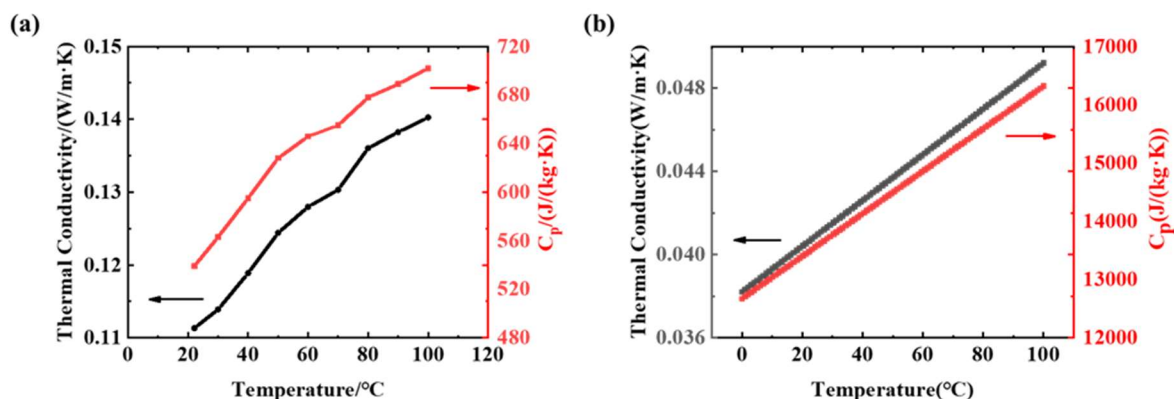


Figure 3. Thermal characteristics of (a) electrodes and (b) separator at the different temperature.

3.1.2 Interfacial EDL structure

In the reversible heat model, the entropy is determined by the probability of ion particles located in a sub-volume (i.e., close to the interfacial electrode-electrolyte area) of the total electrolyte volume and the Boltzmann constant. The entropy of supercapacitor can be described as:

$$S = S^+ + S^- = k_B \left[\ln \left(\frac{V_C^+}{V_0} \right)^{N^+} + \ln \left(\frac{V_C^-}{V_0} \right)^{N^-} \right] = k_B \frac{CU}{e} \left[\ln \left(\frac{V_C^+}{V_0} \right) + \ln \left(\frac{V_C^-}{V_0} \right) \right] \quad (27)$$

, where V_C is the EDL volume, V_0 is the total electrolyte volume, N is the number of ions, k_B is the Boltzmann constant, and C is the capacitance.

The conventional hypothesis is that the EDL structure is solely composed of Helmholtz layer arising from the counter-ion adsorption, and V_0 and V_C can be predicted based on the molecular size of ions and solvents, which is thus used for calculating entropy. This assumption is proved to be valid for dilute electrolytes (e.g., 0.01 M aqueous solutions), which has been widely used for the electro-thermal models. However, the employed commercial organic electrolytes (i.e., 1 M SBP-BF₄/ACN) have considerably high concentration, strong cation-anion correlations and complex ion-solvent interactions (e.g., hydrogen bond and specific adsorption), which probably invalidates the traditional assumptions.

Herein MD simulation is carried out to reveal the microscopic information of organic

electrolytes at the solid/liquid interface for accurately calculating the electrolyte entropy. Electrode carbon atoms are held fixed and rigid during the simulations, defined as Lennard-Jones (L-J) spheres with the parameters proposed by Cheng et al. [42]. The partial charges and force fields for electrolyte ions (SBP⁺ and BF₄⁻) are from Monteiro et al.'s work [43]. The parameters for ACN molecules are chosen from Wu et al.'s work [44]. The interactions between particles (i.e., atoms or ions) can be expressed as a sum of bonded interactions, Coulombic and L-J 12-6 potentials:

$$\begin{aligned}
E_{total} = & \sum_{bonds} K_r (r - r_0)^2 + \sum_{angles} K_\theta (\theta - \theta_0)^2 + \sum_{dihedrals} K_n [1 + d \cos(n\phi)] \\
& + \sum_{i,j} 4\epsilon_{ij} \left[\left(\frac{\sigma_{ij}}{r_{ij}} \right)^{12} - \left(\frac{\sigma_{ij}}{r_{ij}} \right)^6 \right] + \frac{q_i q_j}{r_{ij}}
\end{aligned} \tag{28}$$

, where r_0 and θ_0 represent the equilibrium bond distance and bond angle; K_r , K_θ and K_ϕ denote the bond, angle, and dihedral interaction coefficient; q_i , r_{ij} , ϵ_{ij} and σ_{ij} present the charge of i atom, the distance between i atom and j atom, the minimum energy and the zero energy separation distance, respectively. The LJ parameters for ϵ_{ij} and σ_{ij} are calculated using the Lorentz-Berthelot mixing rules.

Fig. 4(a) shows a representative snapshot of MD simulation model for SBP-BF₄/ACN electrolyte near the charged electrodes. The EDL structure is firstly characterized by the number density distributions. The ion number density $n(z)$ at the position of z perpendicular to electrode surface can be obtained as [45]:

$$n(z) = \frac{1}{L_x L_y \Delta z} \sum_i \delta(z - z_i) \tag{29}$$

, where L_x and L_y present the electrode dimension along the X and Y axes; $\sum_i \delta(z - z_i)$ shows the particle number within a layer of thickness Δz .

Fig 4(b) and (c) show the 1D number density profiles of electrolyte ions near the negative and positive electrodes, respectively. Multilayer electrolyte structring including Helmholtz and diffusion layer is recognized, indicating that conventional model based on the sole Helmholtz region probably cannot describe the entropy accurately. Upon the negative polarization, remarkably high density of SBP⁺ ions (0.00685 # A⁻³) with a small second peak (0.00186 # A⁻³)

³) are developed near the charged surface, while BF_4^- ions without obvious peaks are repelled from the interfacial region due to the strong electrostatic interactions. Especially, ACN solvents accumulate at the buffer region between SBP^+ ions and graphene surface, indicating the full solvation state of SBP^+ ions. As for the positive electrodes, the packing position of the first BF_4^- ion peak (0.00499 \AA^{-3}) is much closer to the charged surface than that of SBP^+ ion due to the smaller ion size and weak solvent interactions. Moreover, BF_4^- ions and ACN molecules almost gather at the identical position, revealing that partial solvent shells are stripped. Similar results can be observed from the 2D number density distributions in Fig. 4(d) and (e). Obvious layer structures are observed for the SBP^+ ions/ACN molecules near the negative polarization and BF_4^- ions/ACN molecules near the positive polarization.

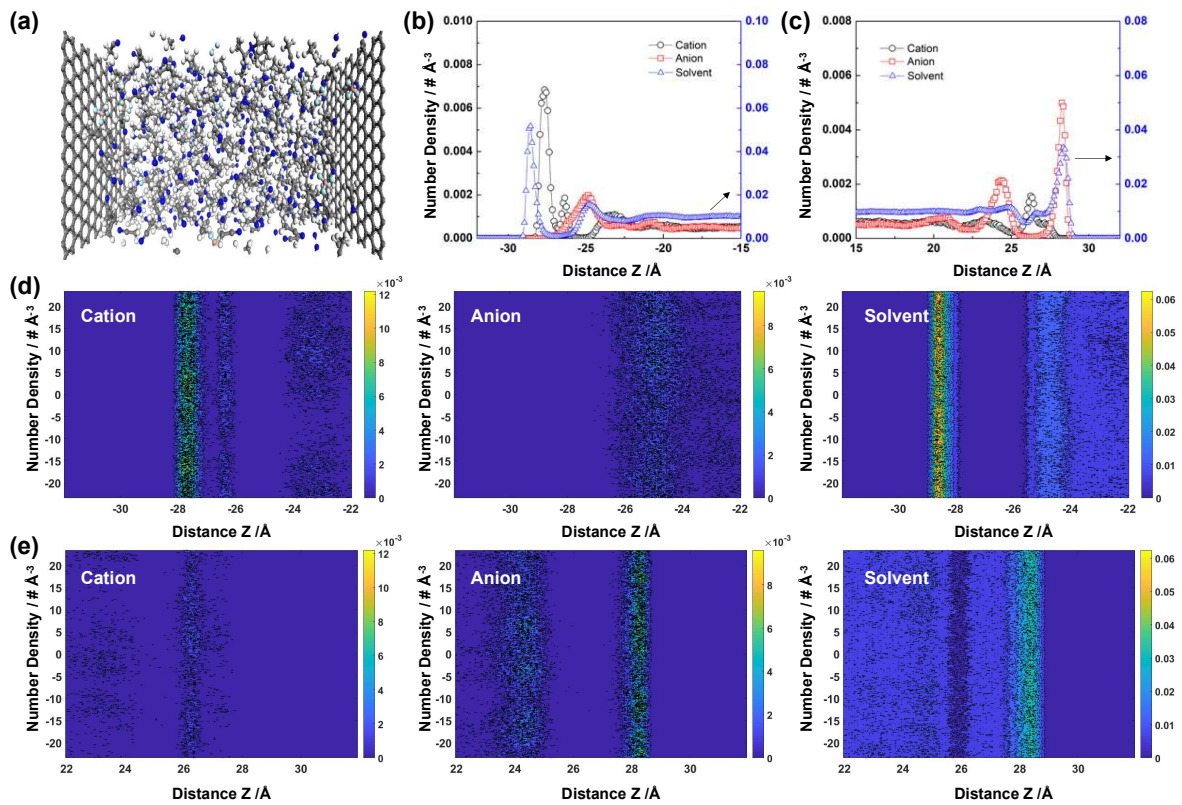


Figure 4. (a) Representative snapshot of MD system. 1D number density profiles near the (b) negative and (c) positive electrodes. 2D number density profiles near the (d) negative and (e) positive electrodes.

3.1.3 Electrical field and capacitive performance

On the basis of the number density, the electrical field and electrical potential distributions can be obtained via the Poisson equation:

$$\nabla_z \left[\varepsilon_0 (\nabla_z \phi(z)) \right] = -\rho(z) \quad (30)$$

With integrating the Poisson equation, the electrical potential $\phi_{\text{total}}(z)$ at the position of z can be expressed as:

$$\phi_{\text{total}}(z) = \frac{\sigma}{\varepsilon_0} z - \frac{1}{\varepsilon_0} \int_0^z (z-z') \rho(z') dz' \quad (31)$$

, where $z = 0$ is the electrode position; σ denotes the electrode charge density, and $\rho(z)$ is the electrolyte charge density.

The electrical field exhibits oscillatory curves within the interfacial EDL area (Fig. 5(a)), which is consistent with the multilayer density manners. Especially, the electrical field is rapidly shielded by the electrolytes and decays to zero within the nanometer thickness EDL area. It is noted that the negative value of electric field can be attributed to the overscreening effect stemming from the charge density $\rho(z)$. Similar trend is observed for the electrical potential distributions (Fig. 5(b)). The electrode capacitance can be obtained as the ratio between the electrode charge density and electrode potential. The areal capacitance of C_{negative} , C_{positive} and C_{total} is calculated to be 4.04, 5.30 and 2.20 $\mu\text{F}/\text{cm}^2$, respectively (Fig. 5(c)). The cathode-anode asymmetry can be reasonably interpreted by the size asymmetry and dipolar charge distribution of ions as well as the different ion-solvent and ion-electrode interactions. Moreover, the self-diffusion coefficients are calculated based on the mean square displacement method to further evaluate the dynamic properties via the following equation:

$$MSD = \frac{1}{3N} \sum_{i=1}^{N-1} \left\langle \left| \vec{r}_i(t) - \vec{r}_i(0) \right|^2 \right\rangle \quad (32)$$

, where $\vec{r}_i(t)$ and $\vec{r}_i(0)$ represent the position of atoms at time t and time 0, respectively; N is the atom number, and the broken bracket denotes the ensemble average. The self-diffusion coefficients for SBP^+ ion, BF_4^- ion, and ACN solvent are calculated to be 10.1, 14.7 and 23.9 $\times 10^{-10} \text{ m}^2/\text{s}$ (Fig. 5(d)).

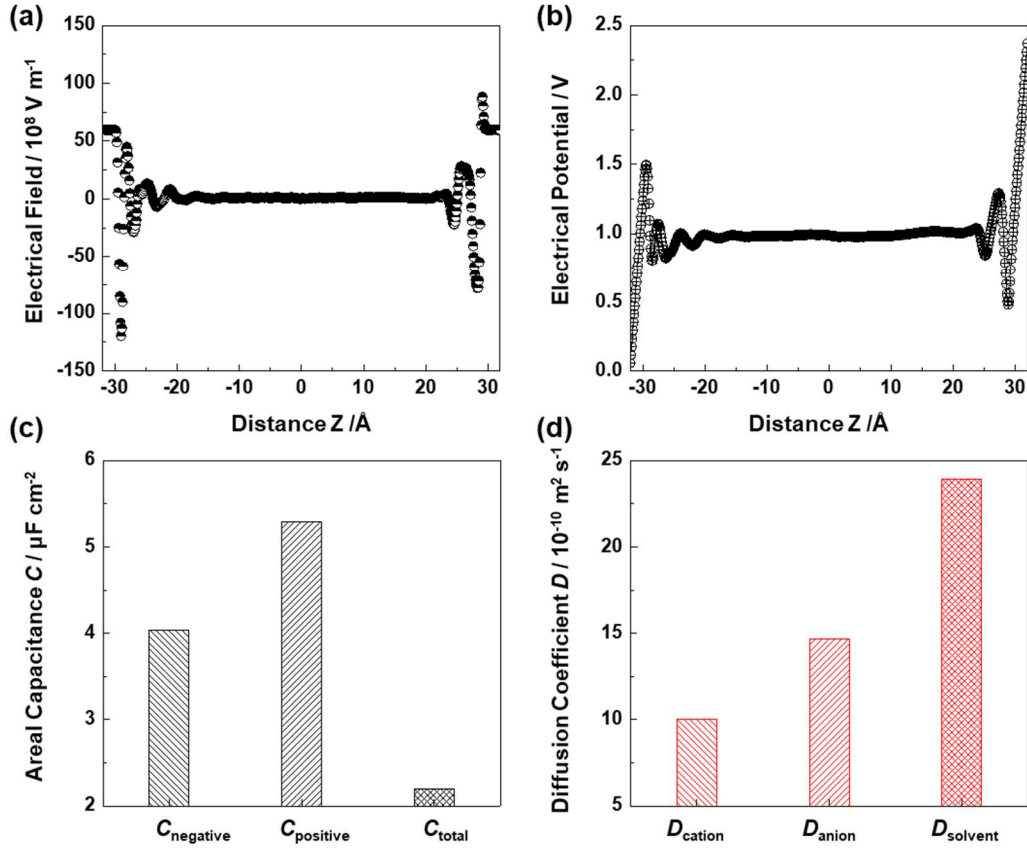


Figure 5. (a) Electrical field and (b) electrical potential distributions near the charged surface. (c) Areal capacitance of C_{negative} , C_{positive} and C_{total} . (d) Diffusion coefficient D for cation, anion and solven molecules.

Based on these results, the effective EDL thickness can be calculated as [46]:

$$d_{EDL} = \frac{\int_{z_0}^{z_1} z^N (z - z_0) \rho(z) dz}{\int_{z_0}^{z_1} z^N \rho(z) dz} \quad (33)$$

, where z_0 is the location of electrode and $\rho(z)$ is the space charge density. The effective EDL thicknesses are 0.810 and 0.771 nm for the negative and positive electrode, respectively. And the EDL volume can be calculated by the following equation:

$$V_C^+ = d_{EDL}^+ \times \delta \times 1/2M, V_C^- = d_{EDL}^- \times \delta \times 1/2M \quad (34)$$

, where M is the mass of activated carbon.

The total electrolyte volume V_0 is predicted from the data of geometric surface, total number of wound layers and thickness of electrodes (aluminum plus activated carbon). Based

on the above results, the improved reversible heat can be described in high fidelity via the following equation:

$$\begin{aligned} \frac{dQ_{rev}}{dt} &= -T \frac{Ck_B}{e} \left[\ln \left(\frac{d_{EDL}^+ \times \delta \times 1/2M}{V_0} \right) + \ln \left(\frac{d_{EDL}^- \times \delta \times 1/2M}{V_0} \right) \right] \frac{dU}{dt} \\ &= -\frac{Tk_B}{e} \left[\ln \left(\frac{1/2 \int_{z_0}^{z_1} z^{N^+} (z-z_0) \rho_+(z) dz}{\int_{z_0}^{z_1} z^{N^+} \rho_+(z) dz} \frac{\delta M}{V_0} \right) + \ln \left(\frac{1/2 \int_{z_0}^{z_1} z^{N^-} (z-z_0) \rho_-(z) dz}{\int_{z_0}^{z_1} z^{N^-} \rho_-(z) dz} \frac{\delta M}{V_0} \right) \right] I \end{aligned} \quad (35)$$

3.2 Mesh Selection

Based on the improved electro-thermal models, finite element method (FEM) simulation is carried out using COMSOL Multiphysics 5.5. A grid independence test is conducted to choose the proper grid size for ensuring high-precise results at low computational costs. Structured hexahedral mesh and unstructured tetrahedral mesh are applied in our computational domain as shown in Fig. 6(a), in which five different sizes of mesh are chosen. The applied current is 10 A, and the initial temperature of supercapacitor is 20 °C with an adiabatic ambient condition. After 5 cycles of constant-current charging and discharging, the temperatures on the supercapacitor at six points under five different grid sizes are presented in Fig. 6(b). A mesh size of 0.00229 mm is chosen in this work in consideration of the high calculation precision and low computational costs.

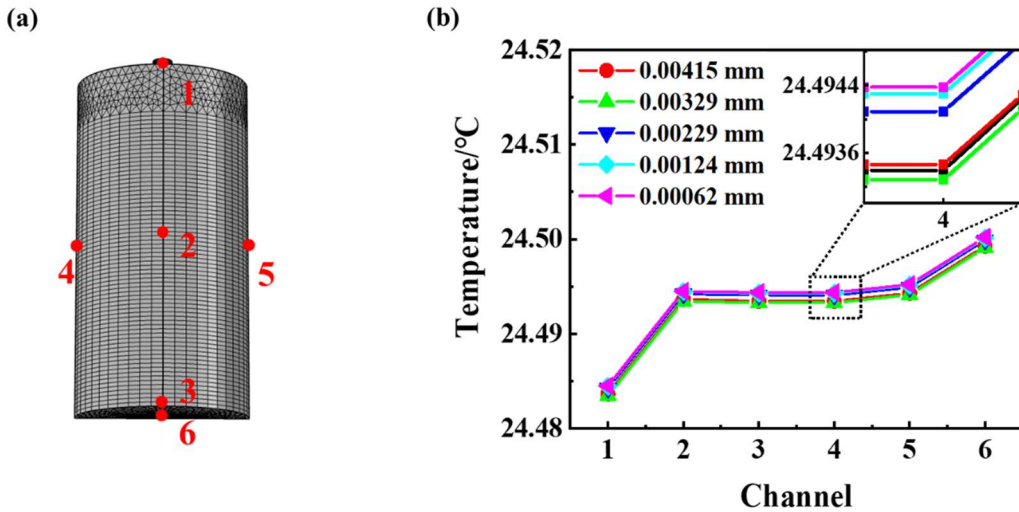


Figure 6. (a) FEM mesh model and distribution of six channels; (b) temperature evolutions of six channels with different mesh sizes.

3.3 Numerical Model Validation

To validate the improved electro-thermal models, two experiments monitoring the temperature variations under thermal insulation and natural convection conditions are conducted. The adiabatic temperature of supercapacitor during the cycling was obtained by the accelerated rate calorimetric (ARC) techniques as shown in Fig. 7(a). The supercapacitor cell under test was placed into a sample pool (diameter of ~ 9 mm) connected to the Galvanostat-Potentiostat. There are two heaters on each side of the furnace to keep the temperature of tested sample and furnace. As presented in Fig. 7(b), the experimental setup is composed of an electrochemical workstation, a 350 F supercapacitor cell, thermocouples and a multiplex temperature recorder. T type thermocouples (with a tolerance of 0.5 °C) were pasted onto the surface of the supercapacitor cell to measure the temperature variations in natural convection condition.

The mean temperature evolution of the supercapacitor cell under thermal insulation and natural convection conditions is shown in Fig. 7(c) and (d). It is noted that the simulation results from the conventional model by Schiffer et al. [8] are also provided for comparison. The temperature rises in a wave profile manner during the charging/discharging cycle, which is consistent with the irreversible and reversible heat generation. Compared with the conventional model, the improved electro-thermal model is able to describe the temperature oscillations more accurately. Details of the temperature evolutions of supercapacitors under thermal insulation and natural convection conditions (Fig. S1) are available in the Supporting Information.

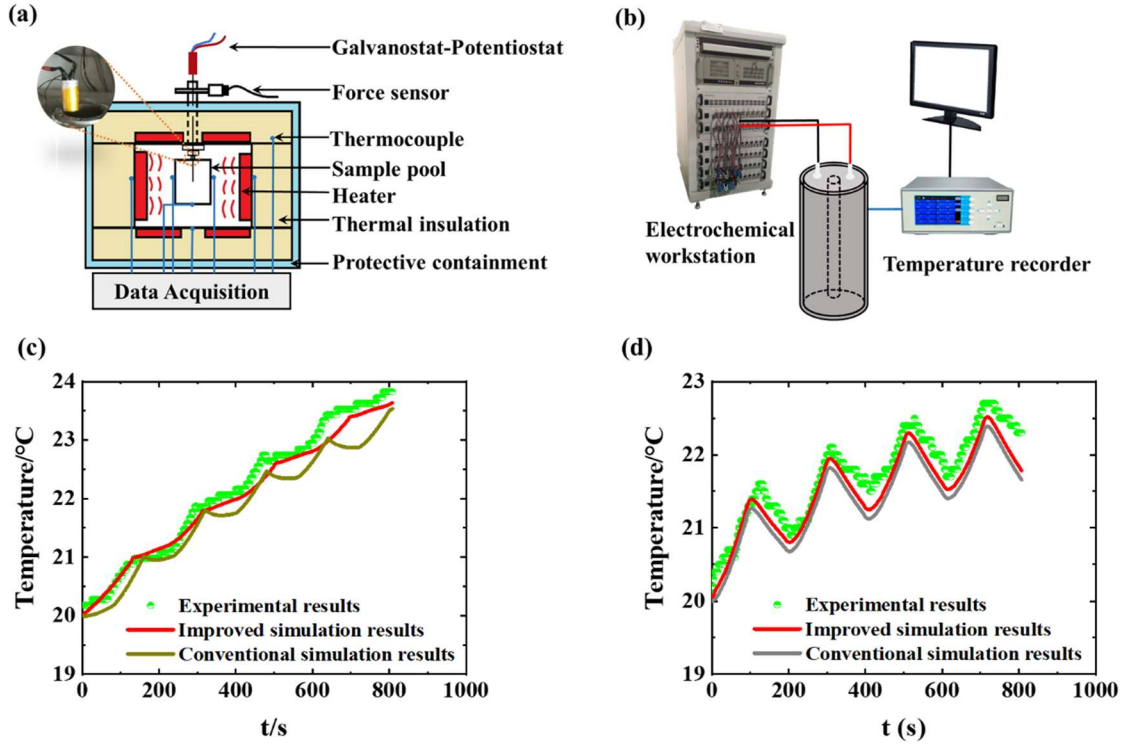


Figure 7. Schematic of experimental setup for supercapacitor temperature measurements under the (a) adiabatic condition and (b) natural convection condition. Comparisons between experiments and simulation results under the (c) thermal insulation and (d) natural convection conditions.

The mean absolute error (MAE) is introduced to quantify the performance of the improved electro-thermal model:

$$MAE = \frac{1}{n} \sum \left| \frac{X_{simulation} - X_{experiment}}{X_{experiment}} \right| \times 100\% \quad (36)$$

The maximum MAE between the improved model and experimental temperature in the adiabatic condition and natural convection condition are calculated to be 2.80% and 1.31% respectively, which is superior to the conventional model. Therefore, these results demonstrate the reliability and precision of our improved model for describing the thermal behaviors of 350 F supercapacitors.

3.4 Data Preparation for LSTM Approach

In these remaining sections, an LSTM RNN is trained to predict the thermal management

performance of supercapacitor modules. The generated heat is removed by an airflow through forced convection due to its advantages of compact structure, cost-effectiveness and environmental-friendly features [47-50]. According to previous work by Gualous et al. [47], a staggered arrangement of supercapacitor cell is chosen in the air cooling system as depicted in Fig. 8. A repeating unit is chosen as the computational domain in consideration of its periodicity, in which the inlet air temperature is set to 20 °C, and supercapacitor cells are labeled as 1-8.

A large amount of high-quality training data is indispensable to ensure the accuracy and generality of deep neural network. The as-obtained simulation results are employed to train and test the LSTM approach based on the CFD simulations. The input and output features for deep learning approach are presented in Table 3. 70% of the 29,000 simulation data for temperature are grouped for training, and 30% are used for evaluating the model structure of LSTM.

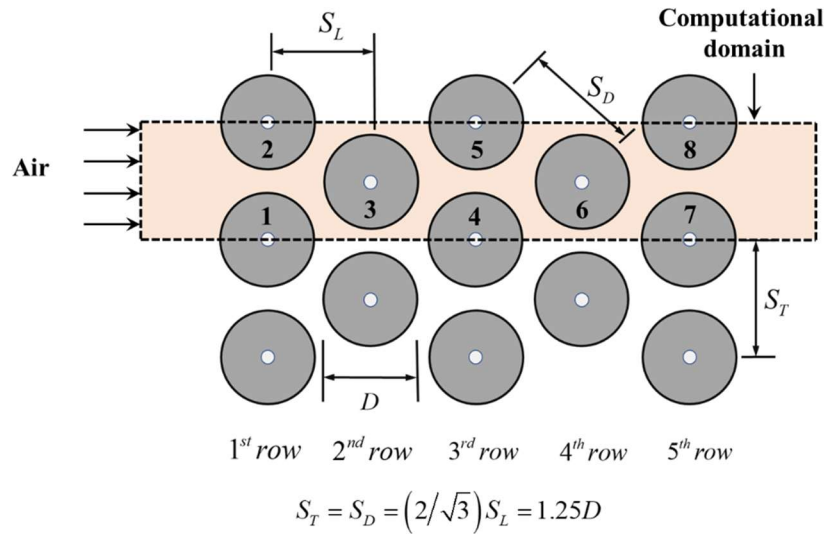


Figure 8. Staggered configuration of supercapacitor cell.

Table 3 The input and output features for deep learning approach.

| | Feature | Value |
|-------|----------------|----------|
| Input | Current rate | 50-100 A |
| | Inlet velocity | 0-1 m/s |
| | Time steps | 0-2000 s |

| | |
|--------|---|
| Output | Temperature of each supercapacitor cell (1, 2, 3, ..., 8) |
|--------|---|

3.5 Optimization of LSTM Approach

In an ANN, the number of neurons in the input layer is equal to the number of input variables, and the number of neurons in the output layer is equal to the number of required output values. Therefore, the appropriate number of hidden layer and neurons plays an important role in the performance of neural network. In this work, three hidden layers are applied and the number of neurons in the hidden layer is determined by trial and error before the ANN training processes.

Fig. 9 shows the results of the unit independence study of LSTM. To determine the number of neurons in the hidden layer, MAE is plotted against the number of neurons in the first hidden layer. Generally, a lower value of MAE indicates a good match between the predicted data and the numerical results. The value of MAE decreases rapidly and converges with the increment of epochs. The network with 2^5 , 2^6 and 2^8 neurons in the first hidden layer has relative lower MAEs. After 300 epochs, MAE value of training and testing database reaches below 0.00875 and 0.00684, respectively. Therefore, the optimal number of neurons in the first hidden layer is chosen as 2^5 .

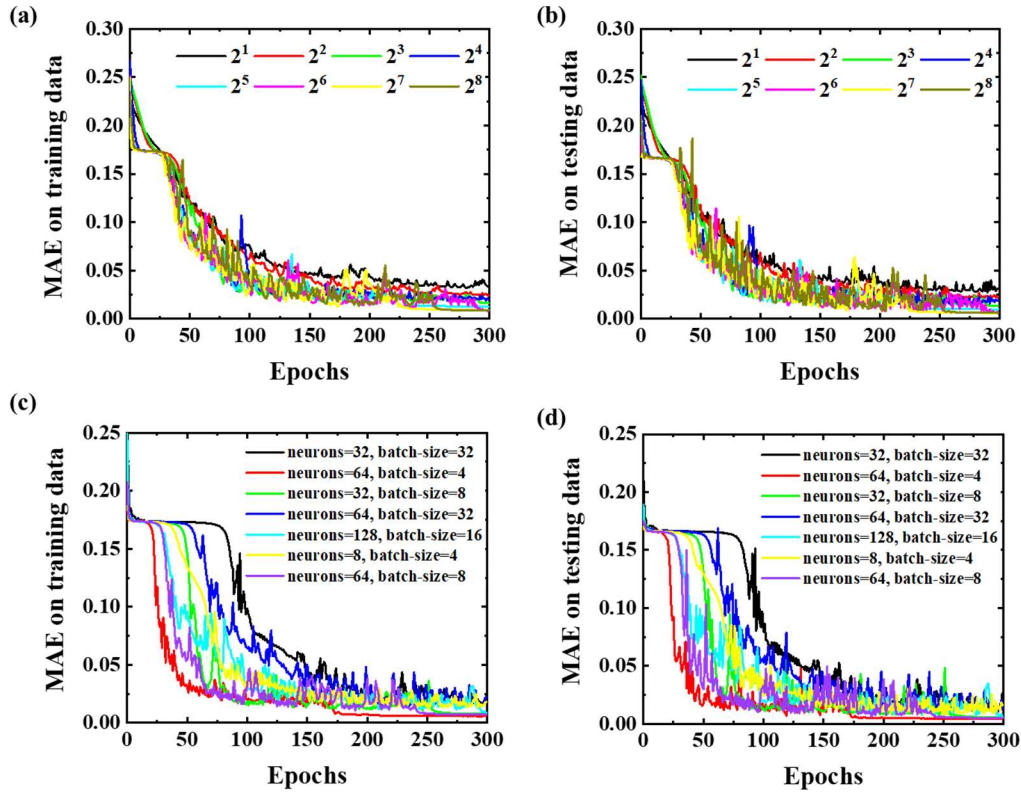


Figure 9. MAE of the (a) training and (b) testing data with different neurons in the first layer as a function of epochs; MAE of the (c) training and (d) testing data as a function of epochs with different hyperparameters.

Moreover, the effect of other hyperparameters (e.g., number of neurons and batch size) on the performance of deep learning approach is further investigated to get optimal results from the LSTM approach. Fig. 9(c) and (d) suggest that the hyperparameters have significant influences on the LSTM performance. It is found that less neurons will have worse generalization performance on the training and testing data, and the most suitable number of neurons is 64; on the other hand, large batch size is more computationally efficient on GPU, but cannot produce better performance. Therefore, the batch size around 4-8 produces quite similar results.

3.6 Forecasting Temperature of Supercapacitor Modules

The performance of the trained LSTM approach can be examined through the scatter plots of LSTM predictions on the testing dataset against the original simulation results. Fig. 10 shows a comparison between ANN predictions and simulation results for a random testing data of 8

supercapacitors. The applied current is 84 A and the inlet velocity is 0.82 m/s. The solid 45° angle line stands for the ideal situation where LSTM predictions perfectly match the simulation results. As shown in Fig. 10(a) - (h), the temperature of 1-8 supercapacitors rises by ~10 K within 2000 s and reaches equilibrium after ~500 s. It is clear that the results of trained network agree well with the numerical simulation data. Fig. 10(i) shows the MAE of all testing data, where the values of MAE are between 0.0003 and 0.0022 for 1-8 supercapacitors. As a result, these training tests demonstrate the generalization of the LSTM approach, which can be used to surrogate the CFD simulations without extensive computational costs.

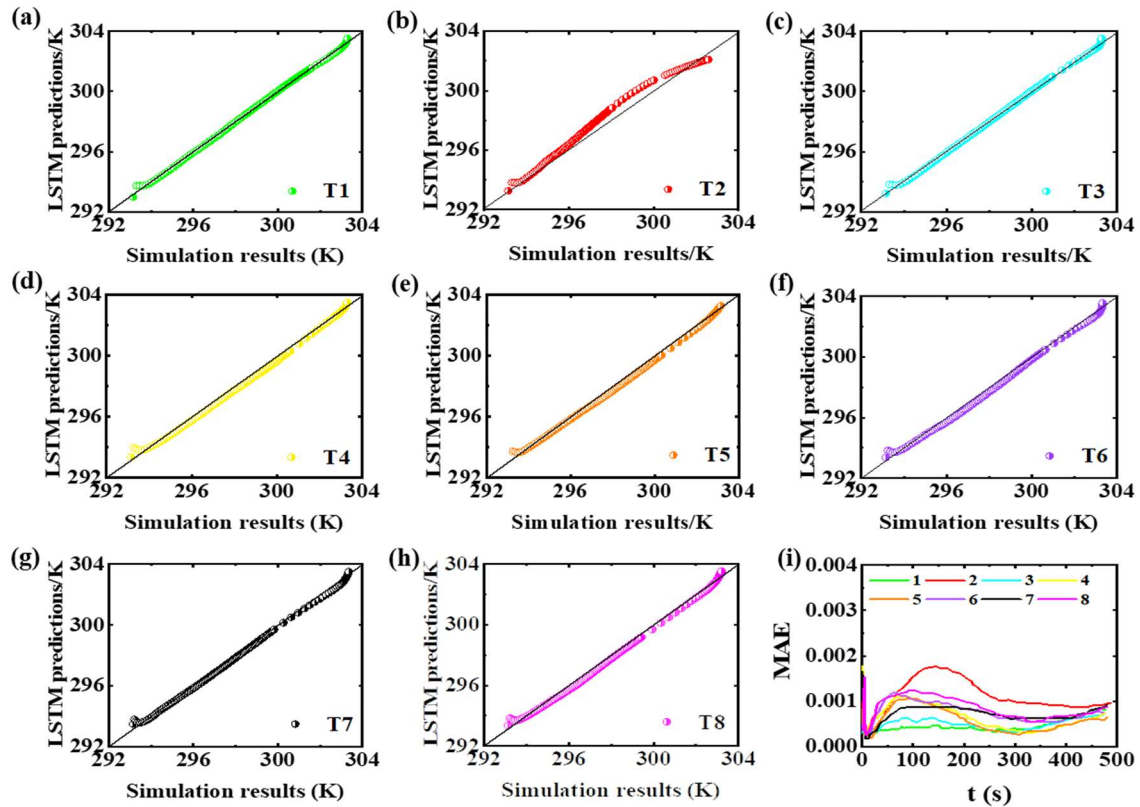


Figure 10. (a-h) Comparison of temperature between the LSTM predictions and simulation results for 1-8 supercapacitors; (i) MAE statistics of overall testing data.

Based on this deep learning approach, the temperature database of supercapacitor module under air cooling is built. Fig. 11 shows the temperature variations of supercapacitors under different operating conditions. This database provides a possibility to quickly estimate the temperature of supercapacitors under different charging-discharging currents, cooling airflow rates and cycle time at computational costs.

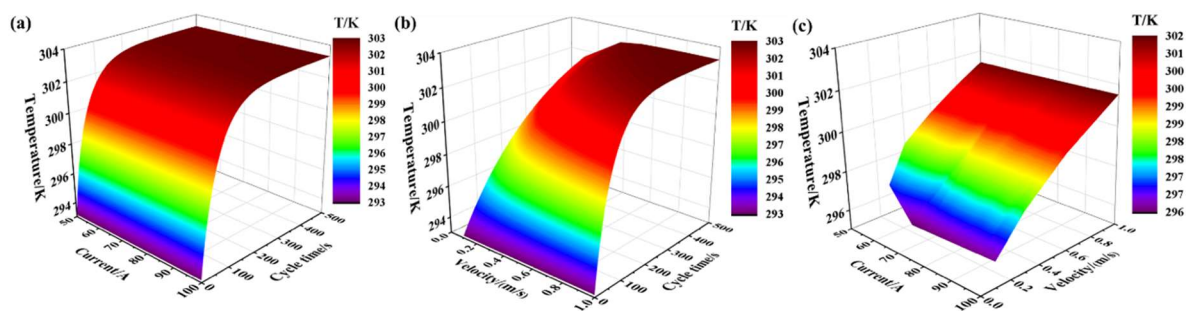


Figure 11. Predicted temperature of supercapacitor module using LSTM at (a) the air inlet velocity of 0.4 m/s, (b) the current rate of 75 A and (c) the cycle time of 100 s.

4. Conclusions

In summary, an LSTM approach with the multiscale coupled electro-thermal model is developed for the first time in predicting the temperature behaviour of supercapacitor modules with air cooling system. A 350 F supercapacitor is fabricated from our proprietary pilot-scale production line. The structural parameters, electrical and thermal properties of electrodes and electrolytes are comprehensively measured to improve the electro-thermal model. Especially, MD is employed to reveal the molecular origin of entropy (e.g., EDL structure, electrical potential distributions, capacitance and diffusion coefficient) for more accurately predicting the reversible heat generation. As a result, the deviation of temperature curves between our improved model and experimentals is obviously decreased ($< 2.80\%$ for adiabatic conditions and $< 1.31\%$ for natural convection conditions).

Deep neural network based on the LSTM approach is trained and developed for the prediction of heat transfer characteristics within supercapacitor module. The data-driven approach takes the current rate, the air inlet velocity, and the cycle time as input features, and temperature of each supercapacitor is set as the output features. The optimal structure of network is determined by trial and error, in which 70% of simulation data are grouped for training, and 30% are used for evaluating the LSTM structure. This enables LSTM predictions with good generalization, high fidelity and well matchment with the simulation results. In the end, deep neural network based on the LSTM approach is trained to build the temperature

database for supercapacitor modules under different operating conditions. This work demonstrates the predictive capability and effectiveness of artificial neural networks in the practical thermal management of energy storage devices.

Acknowledgments

This work was supported by the National Natural Science Foundation of China (No. 51722604 and 51906211), Royal Society Newton Advanced Fellowship (No. 52061130218), and China Postdoctoral Science Foundation (No. 2020T130574 and 2019M662048). Z.B. thanks the National Program for Support of Top-notch Young Professionals. K. O. acknowledges partial support from the Australian Research Council, QUT Centre for Materials Science, and the State Key Laboratory of Clean Energy Utilization Open Fund (No. ZJUCEU2019002).

References

- [1] H.C. Yang, J.Y. Yang, Z. Bo, X. Chen, X.R. Shuai, J. Kong, J.H. Yan, K.F. Cen, Kinetic-Dominated Charging Mechanism within Representative Aqueous Electrolyte-based Electric Double-Layer Capacitors, *J. Phys. Chem. Lett.*, 8(15) (2017) 3703-3710.
- [2] Z.F. Pan, L. An, C.Y. Wen, Recent advances in fuel cells based propulsion systems for unmanned aerial vehicles, *Appl. Energy*, 240 (2019) 473-485.
- [3] P. Simon, Y. Gogotsi, B. Dunn, Where Do Batteries End and Supercapacitors Begin?, *Science*, 343(6176) (2014) 1210-1211.
- [4] Z. Bo, C.Y. Ying, H.C. Yang, S.H. Wu, J.Y. Yang, J. Kong, S.L. Yang, Y.G. Zhou, J.H. Yan, K.F. Cen, Highly Thermo-Conductive Three-Dimensional Graphene Aqueous Medium, *Nano-Micro Lett.*, 12(1) (2020) 12.
- [5] R. Kotz, P.W. Ruch, D. Cericola, Aging and failure mode of electrochemical double layer capacitors during accelerated constant load tests, *J. Power Sources*, 195(3) (2010) 923-928.
- [6] D.H. Lee, U.S. Kim, C.B. Shin, B.H. Lee, B.W. Kim, Y.H. Kim, Modelling of the thermal behaviour of an ultracapacitor for a 42-V automotive electrical system, *J. Power Sources*, 175(1) (2008) 664-668.
- [7] J. Lee, J. Yi, D. Kim, C.B. Shin, K.S. Min, J. Choi, H.Y. Lee, Modeling of the Electrical and Thermal Behaviors of an Ultracapacitor, *Energies*, 7(12) (2014) 8264-8278.
- [8] J. Schiffer, D. Linzen, D.U. Sauer, Heat generation in double layer capacitors, *J. Power Sources*, 160(1) (2006) 765-772.

-
- [9] X.Q. Xu, B.G. Sammakia, D. Jung, T. Eilertsen, Asme, MULTIPHYSICS APPROACH TO MODELING SUPERCAPACITORS FOR IMPROVING PERFORMANCE, Amer Soc Mechanical Engineers, New York, 2012.
- [10] K. Wang, L. Zhang, B.C. Ji, J.L. Yuan, The thermal analysis on the stackable supercapacitor, *Energy*, 59 (2013) 440-444.
- [11] A.L. d'Entremont, L. Pilon, Thermal effects of asymmetric electrolytes in electric double layer capacitors, *J. Power Sources*, 273 (2015) 196-209.
- [12] Y. Parvini, J.B. Siegel, A.G. Stefanopoulou, A. Vahidi, Supercapacitor Electrical and Thermal Modeling, Identification, and Validation for a Wide Range of Temperature and Power Applications, *IEEE Trans. Ind. Electron.*, 63(3) (2016) 1574-1585.
- [13] W. Sarwar, M. Marinescu, N. Green, N. Taylor, G. Offer, Electrochemical double layer capacitor electro-thermal modelling, *J. Energy Storage*, 5 (2016) 10-24.
- [14] X.L. Zhang, W. Wang, J. Lu, L. Hua, J.P. Heng, Reversible heat of electric double-layer capacitors during galvanostatic charging and discharging cycles, *Thermochim. Acta*, 636 (2016) 1-10.
- [15] M. Miller, N.T.M. Baltes, P.M. Rabenecker, M.W. Hagen, J. Tubke, Comprehensive determination of heat generation and thermal modelling of a hybrid capacitor, *J. Power Sources*, 435 (2019) 8.
- [16] Y.S. Li, S.H. Wang, M.N. Zheng, J. Liu, Thermal Behavior Analysis of Stacked-type Supercapacitors with Different Cell Structures, *CSEE J. Power Energy Syst.*, 4(1) (2018) 112-120.
- [17] H. Gualous, H. Louahlia, R. Gallay, Supercapacitor Characterization and Thermal Modelling With Reversible and Irreversible Heat Effect, *IEEE Trans. Power Electron.*, 26(11) (2011) 3402-3409.
- [18] A. Berrueta, I.S. Martin, A. Hernandez, A. Ursua, P. Sanchis, Electro-thermal modelling of a supercapacitor and experimental validation, *J. Power Sources*, 259 (2014) 154-165.
- [19] A. d'Entremont, L. Pilon, First-principles thermal modeling of electric double layer capacitors under constant-current cycling, *J. Power Sources*, 246 (2014) 887-898.
- [20] A. d'Entremont, L. Pilon, Scaling laws for heat generation and temperature oscillations in EDLCs under galvanostatic cycling, *Int. J. Heat Mass Transf.*, 75 (2014) 637-649.
- [21] A. d'Entremont, L. Pilon, First-order thermal model of commercial EDLCs, *Appl. Therm. Eng.*, 67(1-2) (2014) 439-446.
- [22] M. Janssen, R. van Roij, Reversible Heating in Electric Double Layer Capacitors, *Phys. Rev. Lett.*, 118(9) (2017) 6.
- [23] C. Pascot, Y. Dandeville, Y. Scudeller, P. Guillemet, T. Brousse, Calorimetric measurement of the heat generated by a Double-Layer Capacitor cell under cycling, *Thermochim. Acta*, 510(1-2) (2010) 53-60.
- [24] Y. Dandeville, P. Guillemet, Y. Scudeller, O. Crosnier, L. Athouel, T. Brousse, Measuring time-dependent heat profiles of aqueous electrochemical capacitors under cycling, *Thermochim. Acta*, 526(1-2) (2011) 1-8.
- [25] Y. LeCun, Y. Bengio, G. Hinton, Deep learning, *Nature*, 521(7553) (2015) 436-444.
- [26] F. Jia, Y.G. Lei, J. Lin, X. Zhou, N. Lu, Deep neural networks: A promising tool for

fault characteristic mining and intelligent diagnosis of rotating machinery with massive data, *Mech. Syst. Signal Proc.*, 72-73 (2016) 303-315.

[27] C. Fan, F. Xiao, Y. Zhao, A short-term building cooling load prediction method using deep learning algorithms, *Appl. Energy*, 195 (2017) 222-233.

[28] G. Suryanarayana, J. Lago, D. Geysen, P. Aleksiejuk, C. Johansson, Thermal load forecasting in district heating networks using deep learning and advanced feature selection methods, *Energy*, 157 (2018) 141-149.

[29] A. Rahman, A.D. Smith, Predicting heating demand and sizing a stratified thermal storage tank using deep learning algorithms, *Appl. Energy*, 228 (2018) 108-121.

[30] L. Yang, W. Dai, Y. Rao, M.K. Chyu, Optimization of the hole distribution of an effusively cooled surface facing non-uniform incoming temperature using deep learning approaches, *Int. J. Heat Mass Transf.*, 145 (2019) 10.

[31] Y. Liu, N. Dinh, Y. Sato, B. Niceno, Data-driven modeling for boiling heat transfer: Using deep neural networks and high-fidelity simulation results, *Appl. Therm. Eng.*, 144 (2018) 305-320.

[32] D. Erhan, Y. Bengio, A. Courville, P.A. Manzagol, P. Vincent, S. Bengio, Why Does Unsupervised Pre-training Help Deep Learning?, *J. Mach. Learn. Res.*, 11 (2010) 625-660.

[33] Y.S. Chen, Z.H. Lin, X. Zhao, G. Wang, Y.F. Gu, Deep Learning-Based Classification of Hyperspectral Data, *IEEE J. Sel. Top. Appl. Earth Observ. Remote Sens.*, 7(6) (2014) 2094-2107.

[34] J. Schmidhuber, Deep learning in neural networks: An overview, *Neural Netw.*, 61 (2015) 85-117.

[35] X.S. Hu, S.E. Li, Y.L. Yang, Advanced Machine Learning Approach for Lithium-Ion Battery State Estimation in Electric Vehicles, *IEEE Trans. Transp. Electrification*, 2(2) (2016) 140-149.

[36] T. Zahid, K. Xu, W.M. Li, Machine learning an alternate technique to estimate the state of charge of energy storage devices, *Electron. Lett.*, 53(25) (2017) 1665-1666.

[37] T. Zahid, K. Xu, W.M. Li, C.M. Li, H.Z. Li, State of charge estimation for electric vehicle power battery using advanced machine learning algorithm under diversified drive cycles, *Energy*, 162 (2018) 871-882.

[38] S. Hochreiter, J. Schmidhuber, Long short-term memory, *Neural Comput.*, 9(8) (1997) 1735-1780.

[39] F.J. Ordonez, D. Roggen, Deep Convolutional and LSTM Recurrent Neural Networks for Multimodal Wearable Activity Recognition, *Sensors*, 16(1) (2016) 25.

[40] K. Greff, R.K. Srivastava, J. Koutnik, B.R. Steunebrink, J. Schmidhuber, LSTM: A Search Space Odyssey, *IEEE Trans. Neural Netw. Learn. Syst.*, 28(10) (2017) 2222-2232.

[41] H. Gualous, D. Bouquain, A. Berthon, J.M. Kauffmann, Experimental study of supercapacitor serial resistance and capacitance variations with temperature, *J. Power Sources*, 123(1) (2003) 86-93.

[42] A. Cheng, W.A. Steele, COMPUTER-SIMULATION OF AMMONIA ON GRAPHITE .1. LOW-TEMPERATURE STRUCTURE OF MONOLAYER AND BILAYER FILMS, *J. Chem. Phys.*, 92(6) (1990) 3858-3866.

[43] M.J. Monteiro, F.F.C. Bazito, L.J.A. Siqueira, M.C.C. Ribeiro, R.M. Torresi, Transport coefficients, Raman spectroscopy, and computer simulation of lithium salt solutions

in an ionic liquid, *J. Phys. Chem. B*, 112(7) (2008) 2102-2109.

[44] X.P. Wu, Z.P. Liu, S.P. Huang, W.C. Wang, Molecular dynamics simulation of room-temperature ionic liquid mixture of bmim BF₄ and acetonitrile by a refined force field, *Phys. Chem. Chem. Phys.*, 7(14) (2005) 2771-2779.

[45] H.C. Yang, Z. Bo, J.H. Yan, K.F. Cen, Influence of wettability on the electrolyte electrosorption within graphene-like nonconfined and confined space, *Int. J. Heat Mass Transf.*, 133 (2019) 416-425.

[46] H.C. Yang, X.L. Zhang, J.Y. Yang, Z. Bo, M. Hu, J.H. Yan, K.F. Cen, Molecular Origin of Electric Double-Layer Capacitance at Multilayer Graphene Edges, *J. Phys. Chem. Lett.*, 8(1) (2017) 153-160.

[47] I. Voicu, H. Louahlia, H. Gualous, R. Gallay, Thermal management and forced air-cooling of supercapacitors stack, *Appl. Therm. Eng.*, 85 (2015) 89-99.

[48] X.L. Zhang, W. Wang, H.X. He, L. Hua, J.P. Heng, Optimization of the air-cooled supercapacitor module compartment for an electric bus, *Appl. Therm. Eng.*, 112 (2017) 1297-1304.

[49] I. Voicu, R. Rizk, H. Louahlia, F. Bode, H. Gualous, Experimental and numerical study of supercapacitors module with air-cooling, *Appl. Therm. Eng.*, 159 (2019) 11.

[50] Z.C. Zhang, E. Lau, C. Botting, M. Bahrami, Naturally cooled heat sinks for battery chargers, *Int. J. Heat Mass Transf.*, 147 (2020) 13.